

# Hofstadter-Herman Visualization as a Diagnostic Tool for Systematic Effects in Electromagnetic Form Factor Extractions

Tyler Williams,<sup>1</sup> Jennifer Rittenhouse West,<sup>2,3</sup> D. W. Higinbotham,<sup>4</sup> and Fatiha Benmokhtar<sup>1,\*</sup>

<sup>1</sup>*Department of Physics, Duquesne University, Pittsburgh, PA 15282*

<sup>2</sup>*INFN Turin Section, Turin, Italy 10125*

<sup>3</sup>*Department of Physics, University of Turin, Turin, Italy 10125*

<sup>4</sup>*Thomas Jefferson National Accelerator Facility, Newport News, VA 23606*

(Dated: November 26, 2025)

The internal charge and magnetization distributions of the proton are characterized by electromagnetic form factors  $G_E$  and  $G_M$ . They are experimentally extracted via Rosenbluth separation, which measures the elastic scattering of electrons and protons at multiple beam energies and angles at fixed momentum transfer  $Q^2$ . Conventionally, form factor values are obtained by plotting reduced cross sections against the virtual photon polarization parameter  $\epsilon$  and then extracting the slope and intercept of the best fit lines. An alternative visualization method, proposed by Hofstadter and Herman in 1960, plots  $G_M^2$  vs.  $G_E^2$  curves instead. The best fit values of  $G_E^2$  and  $G_M^2$  are immediately visible from the intersection region of the curves and their uncertainty bands. In this work, we apply both conventional and Hofstadter-Herman visualizations to classic 1994 SLAC elastic scattering data. We demonstrate that the Hofstadter-Herman method reveals previously obscured regions of form factor parameter space and highlights subtle experimental discrepancies among data sets. Our results motivate adopting this visualization method as a routine diagnostic cross-check at the Electron–Ion Collider and elsewhere, to flag normalization shifts and related adjustments before they enter global fits.

## I. INTRODUCTION

Nucleon electromagnetic form factors characterize how electric charge and magnetization are distributed within the proton and neutron, providing fundamental insight into their internal structure [1–5]. In Quantum Electrodynamics (QED), elastic electron–nucleon scattering occurs at leading order through the exchange of a single virtual photon carrying four-momentum  $q$ , with invariant four-momentum transfer squared defined to be  $Q^2 \equiv -q^2$  [6–8]. Experimentally, form factors are extracted from elastic scattering of charged leptons off nucleon targets. Liquid hydrogen targets are typically used for proton measurements, while neutron information is obtained from quasielastic scattering on light nuclei such as deuterium or  $^3\text{He}$ . Elastic  $ep$  scattering has played a central role in the study of the internal structure of the proton for more than seventy years [9–11].

Elastic scattering from a spin- $\frac{1}{2}$  nucleon requires two independent Lorentz-invariant form factors to describe its electromagnetic current. These are expressed as the Sachs electric and magnetic form factors,  $G_E(Q^2)$  and  $G_M(Q^2)$ . In 1962 Sachs showed that, in the Breit frame and in the nonrelativistic limit,  $G_E(Q^2)$  and  $G_M(Q^2)$  can be interpreted as Fourier transforms of the nucleon's spatial charge and magnetization densities [8]. The unpolarized elastic scattering cross section depends on both form factors and their relative weights vary with scattering angle and beam energy at fixed  $Q^2$ .

The standard procedure for separating  $G_E$  and  $G_M$  from unpolarized cross sections is the Rosenbluth (or

longitudinal–transverse) separation. Measurements are taken at fixed  $Q^2$  but with different combinations of beam energies and scattering angles. The data are then plotted as reduced cross sections versus the virtual photon polarization parameter  $\epsilon$  (a known kinematic function of  $Q^2$  and  $\theta$ , see Section II), and a linear fit yields  $G_E^2$  and  $G_M^2$  as the slope and intercept of the line. Although robust in principle, this method can conceal systematic inconsistencies between data sets by fitting data to a line and then extracting the form factors.

An alternative visualization was proposed by Hofstadter and Herman in 1960 [11]. Instead of plotting reduced cross sections, they plotted data directly in form factor space, where each data point with uncertainties at fixed  $Q^2$  corresponds to an allowed band of form factor values. When multiple measurements at the same  $Q^2$  but different beam energies are displayed together, the overlapping region of these bands directly identifies the consistent form factor pair. Hofstadter and Herman originally presented their visualization in the Dirac–Pauli form factor plane ( $F_1, F_2$ ). We apply the same concept in the Sachs basis ( $G_E^2, G_M^2$ ) [8].

In this work, we apply both the conventional Rosenbluth plotting method and the Hofstadter–Herman visualization to the 1994 SLAC elastic–scattering data of Andivahis *et al.* [12]. We show that the Hofstadter–Herman approach reveals subtle tensions in the data, most notably, tension between normalized and unnormalized data sets that are not apparent in traditional Rosenbluth plots. Comparison with the Jefferson Lab Global Fit (see Appendix A of [13]) suggests that an applied 4% normalization correction in the original SLAC analysis does not improve agreement with modern extractions. This study highlights the diagnostic power of

\* Contact person: benmokhtar@duq.edu

visualizing data directly in form factor space for uncovering systematic effects and data set inconsistencies, which is relevant for the Electron-Ion Collider [14, 15].

## II. THEORETICAL FOUNDATIONS

Electromagnetic form factors provide a quantitative description of the spatial distributions of electric charge and magnetization within the proton. The electric form factor,  $G_E(Q^2)$ , reflects the electric charge distribution, while the magnetic form factor,  $G_M(Q^2)$ , characterizes the magnetization profile. Both are functions of the squared four-momentum transfer,  $Q^2$ , and are fundamental to understanding the internal structure of the nucleon [1–3]. These form factors are directly related to the underlying quark dynamics, as the proton's electric charge is carried by its constituent quarks and antiquarks. By analyzing the behavior of  $G_E$  and  $G_M$  over a range of  $Q^2$  values, one can infer information about the spatial configuration and behavior of confined quarks, as well as estimate key properties such as the proton's radius [16, 17] and shape [18, 19].

As mentioned previously, elastic electron-proton scattering forms the experimental basis for determining the proton's electromagnetic form factors [10]. In this process, an incident electron beam of known energy interacts with a stationary proton target, resulting in a scattered electron and a recoiling proton. Crucially, no energy is transferred to the internal degrees of freedom of the proton; while the proton recoils with kinetic energy, it remains in its ground state, distinguishing elastic from inelastic scattering, where the proton can be excited to resonances or break apart.

In the single photon exchange approximation, the unpolarized differential cross section can be written in the form [7]

$$\frac{d\sigma}{d\Omega} = \left( \frac{d\sigma}{d\Omega} \right)_{\text{ns}} \left[ \frac{G_E^2(Q^2) + \tau G_M^2(Q^2)}{1 + \tau} + 2\tau G_M^2(Q^2) \tan^2\left(\frac{\theta}{2}\right) \right]. \quad (1)$$

Here,  $(d\sigma/d\Omega)_{\text{ns}}$  is the cross section for a point-like spinless proton (i.e., “no structure,” also known as Mott scattering),  $M_p = 0.938$  GeV is the proton mass,  $\tau = Q^2/4M_p^2$ , and  $\theta$  is the electron scattering angle. We work with natural units in which  $\hbar = c = 1$ . This formulation underpins the Rosenbluth separation technique, which allows an independent extraction of the electric ( $G_E$ ) and magnetic ( $G_M$ ) form factors by systematically varying the scattering angle while maintaining a fixed  $Q^2$ .

In the Rosenbluth separation experiments performed at SLAC, high-energy electron beams, typically in the range of 1.6–8.0 GeV, were directed at liquid hydrogen targets. The angular distribution of scattered electrons was measured using precision magnetic spectrometers, al-

lowing for accurate determination of the differential cross sections across a broad range of momentum transfers.

### Conventional Rosenbluth Visualization

Form factors are typically extracted using the Rosenbluth separation technique. This method involves determining the differential cross section at fixed  $Q^2$  from data taken at different beam energies and scattering angles. Data are conventionally plotted as  $\sigma_R \epsilon (1 + \tau)$  versus virtual photon polarization  $\epsilon$  at fixed  $Q^2$ . In this case, the slope corresponds to  $G_E^2$  and the intercept to  $\tau G_M^2$ , allowing both form factors to be algebraically extracted from a straight-line fit.

A modification of the conventional method plots the reduced cross section after dividing both sides of the equation by the square of the magnetic dipole form  $G_D^2$ , resulting in the following equation

$$\frac{\sigma_R}{G_D^2(Q^2)} \equiv \left( \frac{d\sigma}{d\Omega} \right) \frac{(1 + \tau)}{5.18} \frac{\epsilon}{\tau} \frac{E^3 \sin^4\left(\frac{\theta}{2}\right)}{E' \cos^2\left(\frac{\theta}{2}\right)} \left( 1 + \frac{Q^2}{0.71} \right)^4 \quad (2)$$

where  $G_D(Q^2) = \left( 1 + \frac{Q^2}{0.71} \right)^{-2}$  with numerical factor 0.71 from fitting to existing 1994 data. We use this equation in our example of conventional Rosenbluth plots in order to illustrate the method used in 1994 by SLAC [12], shown as  $\sigma_R/G_D^2$  vs.  $\epsilon$  in Figure 1. The electromagnetic form factors obtained in this method are proportional to the slope and y-intercept of the best-fit line.

The different choices of plotting variables and form factor extractions emphasize the point that conventional visualization methods can be confusing and obscure the physical parameters. The fitting process itself smooths out potentially important information from the data.

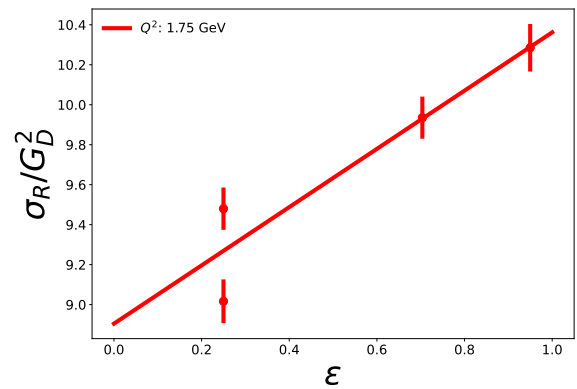


FIG. 1. An example of a standard Rosenbluth separation method plot, here at  $Q^2 = 1.75$  GeV.

### Hofstadter-Herman Visualization Method

A geometric visualization method was proposed by Richard Hofstadter and Robert Herman in 1960. They suggested that the form factor data could be displayed more effectively by plotting allowed regions in form factor space, with uncertainty bands drawn around each form factor curve. The intersection of the bands gives the form factor values directly.

In order to derive the relationship between  $G_E^2$  and  $G_M^2$  for the Hofstadter-Herman plots, it is useful to rewrite Eq. 1 to make its linear dependence on the virtual photon polarization parameter  $\epsilon$  explicit. Rearranging to isolate the  $\epsilon$ -dependence yields

$$\frac{d\sigma}{d\Omega} = \frac{\sigma_{\text{ns}}}{\epsilon(1+\tau)} (\tau G_M^2(Q^2) + \epsilon G_E^2(Q^2)) \quad (3)$$

A reminder that  $\tau$  is defined as

$$\tau = \frac{Q^2}{4M_p^2} \quad (4)$$

and  $\epsilon$  is

$$\epsilon = \frac{1}{1 + 2(1 + \tau) \tan^2(\frac{\theta}{2})}. \quad (5)$$

The reduced cross section is given by

$$\sigma_R = \frac{d\sigma/d\Omega}{\sigma_{\text{ns}}} \quad (6)$$

where the no-structure (Mott) cross section is

$$\sigma_{\text{ns}} = \frac{\alpha^2 \cos^2(\frac{\theta}{2})}{4E^2 \sin^4(\frac{\theta}{2})} \frac{E'}{E}. \quad (7)$$

Here  $E$  and  $E'$  denote the incident and scattered electron energies in the laboratory frame.

Substituting and rearranging algebraically, we find

$$\sigma_R = \frac{1}{\epsilon(1+\tau)} (\tau G_M^2(Q^2) + \epsilon G_E^2(Q^2)) \quad (8)$$

which yields

$$G_E^2(Q^2) = \sigma_R(1 + \tau) - \frac{\tau}{\epsilon} G_M^2(Q^2). \quad (9)$$

Since unpolarized cross sections depend only on  $G_E^2$  and  $G_M^2$ , they determine only the magnitudes of the form factors, not their signs. Using Eq. 9, the Hofstadter-Herman plot is constructed by scanning a range of  $G_M^2(Q^2)$  values to determine the corresponding  $G_E^2(Q^2)$  values.

In the original Hofstadter-Herman construction, each measurement defined an ellipse in the Dirac-Pauli form factor plane ( $F_1, F_2$ ); the intersection of several such ellipses identified the consistent form factor pair. In the Sachs representation used here, those loci become nearly

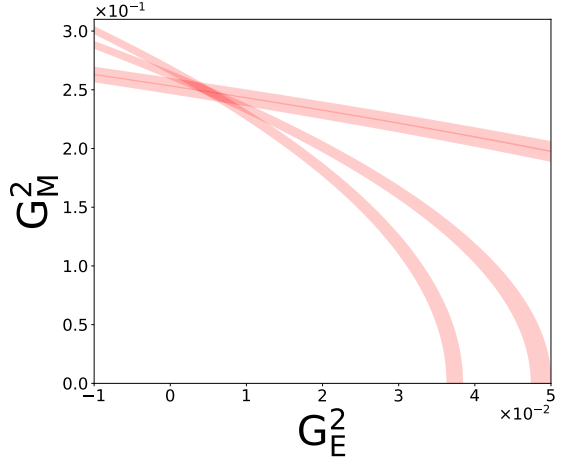


FIG. 2. An example of the Hofstadter-Herman visualization method, here at  $Q^2 = 1.75$  GeV.

straight bands in  $(G_E^2, G_M^2)$  space. The overlap region of these bands identifies the pair  $(G_E^2, G_M^2)$  that best satisfies all measurements at the same  $Q^2$  (and also the magnitudes  $|G_E|$  and  $|G_M|$  for unpolarized scattering). Figure 2 shows an example Hofstadter-Herman visualization plot.

### III. GRAPHICAL ANALYSIS

In accordance with the Hofstadter-Herman method, graphical representations were constructed using the published cross section and kinematic SLAC data from Andivahis et al. [12]. The graphs were generated using Python, specifically employing the NumPy and Matplotlib libraries. As an initial validation step, the reduced cross section graph presented in the original SLAC publication was reproduced. This served to confirm the accuracy and reliability of the computational framework. The reproduction was achieved with high fidelity, exhibiting small deviations that are addressed in the following subsection. Following this verification, the code was adapted to express the algebraic relation between  $G_E^2(Q^2)$  and  $G_M^2(Q^2)$ , which was then used to generate Hofstadter-Herman plots. Each band in these plots corresponds to one measurement at a given beam energy and scattering angle, with the band width reflecting the experimental uncertainty in  $\sigma_R$ . The intersection of multiple bands identifies the consistent pair of form-factor values for that  $Q^2$ . This approach enables direct visualization of the form factors' behavior, eliminating the need to infer results from linear fits.

## SLAC Data

We now apply this framework to the 1994 SLAC dataset. The cross section graph originally published by SLAC was successfully reconstructed, reproducing the overall structure of the 1994 result with minor deviations. These small differences arise from a normalization correction applied to a subset of the data. According to the SLAC report, measurements obtained with the 1.6 GeV spectrometer were scaled by approximately 4% to achieve consistency with data collected using the higher energy spectrometers. Figure 3 shows the reconstructed SLAC plot including this normalization factor.

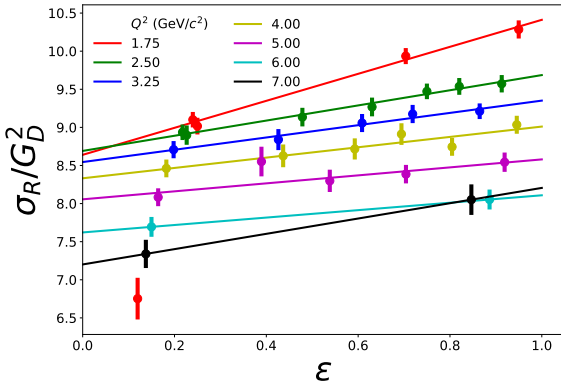


FIG. 3. Conventional plot of normalized SLAC data reflecting a 4% normalization applied to the 1.6 GeV spectrometer subset, as in the original analysis; see text for discussion.

For comparison, Figure 4 displays the same dataset before normalization. Although the visual differences between the two plots are modest, they illustrate how even small normalization shifts can influence the apparent consistency among measurements. Applying the SLAC-recommended normalization yields a reconstructed graph

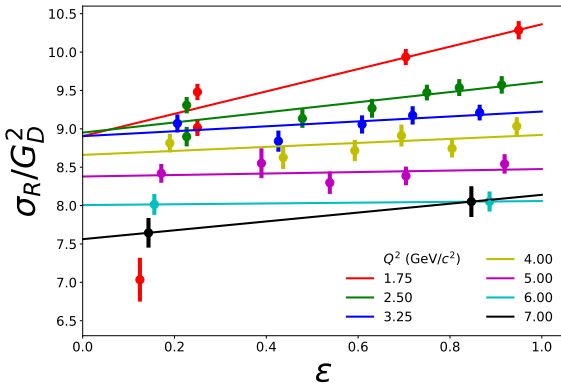


FIG. 4. Conventional plot of SLAC data without the normalization adjustment, illustrating the original measurements without the applied 4% normalization to the 1.6 GeV spectrometer subset.

in close agreement with the published result.

The same dataset was then reanalyzed using the Hofstadter-Herman visualization technique, producing two distinct graphical representations: one incorporating the 4% correction (Figure 5) and one based on the unadjusted data (Figure 6). A visual comparison of both with the Jefferson Lab Global Fit (Appendix A of [13]) indicates that the global fit curve aligns more closely with the unnormalized data, suggesting that the original uncorrected measurements better reflects the underlying physical behavior.

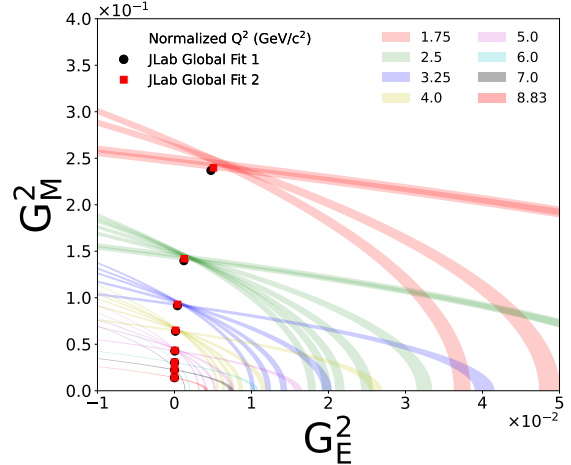


FIG. 5. Hofstadter-Herman plot of normalization-adjusted SLAC data.

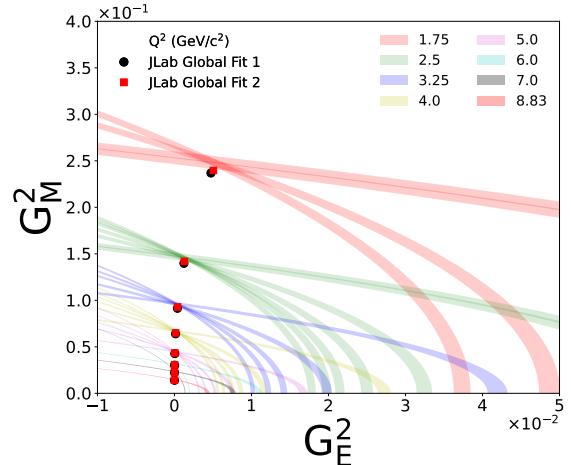


FIG. 6. Hofstadter-Herman plot of unadjusted SLAC data.

This notable discrepancy observed between the 1994 data and the Jefferson Lab Global Fit is difficult to discern in conventional Rosenbluth separation plots. In contrast, the Hofstadter-Herman visualization presents the data directly, as overlapping bands of allowed form factor values at fixed  $Q^2$  across different beam energies. Within

this representation, the consistent form factor values correspond to the region where the bands intersect, and the Global Fit curve can be seen to pass through or deviate from this region. This direct visualization enhances the interpretability of the data and underscores the limitations of relying solely on global fits without reference to the underlying experimental distributions.

#### IV. FUTURE APPLICATIONS AND CONCLUSIONS

We have revisited classic SLAC elastic  $ep$  scattering data using both conventional Rosenbluth plots and the Hofstadter-Herman visualization method. The latter presents the form factors directly, rather than through the usual two-step procedure of fitting a line to the data and then extracting  $G_E^2$  and  $G_M^2$  from the slope and intercept. This approach can reveal subtle normalization inconsistencies that are difficult to detect in traditional plots. In the SLAC dataset, a 4% normalization correction applied to the 1.6 GeV spectrometer data in the original SLAC analysis shifted the measurements away from the region favored by modern global fits, an effect seen in the Hofstadter-Herman plots but masked in the conventional plots. The shift suggests that the uncor-

rected data more accurately reflect the underlying form factor behavior.

By mapping the allowed  $(G_E^2, G_M^2)$  regions directly, Hofstadter-Herman visualization can make certain inconsistencies between data sets apparent, particularly those arising from normalization or calibration shifts that may remain hidden in linearized analyses. Such geometric cross-checks can complement standard analysis techniques at future facilities, including the Electron–Ion Collider, by helping to identify normalization offsets or other subtle biases before they propagate into global fits. More broadly, this work underscores the continuing value of direct, geometry-based representations of form factor data for assessing the internal consistency of high-precision measurements.

#### V. ACKNOWLEDGEMENTS

T.W and F.B acknowledge support from the National Science Foundation, Award No.Benmokhtar-2310067. J.R.W. acknowledges support from the Istituto Nazionale di Fisica Nucleare (INFN) Turin, Grant No. 25864. This research was funded in part by the Department of Energy grant number DE-AC05-06OR23177.

---

[1] Z. Ye, J. Arrington, R. J. Hill, and G. Lee, “Proton and Neutron Electromagnetic Form Factors and Uncertainties,” *Phys. Lett. B*, vol. 777, pp. 8–15, 2018.

[2] Y.-H. Lin, H.-W. Hammer, and U.-G. Meißner, “New Insights into the Nucleon’s Electromagnetic Structure,” *Phys. Rev. Lett.*, vol. 128, no. 5, p. 052002, 2022.

[3] W. M. Alberico, S. M. Bilenky, C. Giunti, and K. M. Graczyk, “Electromagnetic form factors of the nucleon: New Fit and analysis of uncertainties,” *Phys. Rev. C*, vol. 79, p. 065204, 2009.

[4] J. C. Bernauer *et al.*, “Electric and magnetic form factors of the proton,” *Phys. Rev. C*, vol. 90, no. 1, p. 015206, 2014.

[5] G. Kubon *et al.*, “Precise neutron magnetic form-factors,” *Phys. Lett. B*, vol. 524, pp. 26–32, 2002.

[6] M. E. Rose, “The Charge Distribution in Nuclei and the Scattering of High Energy Electrons,” *Phys. Rev.*, vol. 73, pp. 279–284, 1948.

[7] M. N. Rosenbluth, “High Energy Elastic Scattering of Electrons on Protons,” *Phys. Rev.*, vol. 79, pp. 615–619, 1950.

[8] R. G. Sachs, “High-Energy Behavior of Nucleon Electromagnetic Form Factors,” *Phys. Rev.*, vol. 126, pp. 2256–2260, 1962.

[9] R. Hofstadter and R. W. McAllister, “Electron Scattering From the Proton,” *Phys. Rev.*, vol. 98, pp. 217–218, 1955.

[10] C. F. Perdrisat, V. Punjabi, and M. Vanderhaeghen, “Nucleon Electromagnetic Form Factors,” *Prog. Part. Nucl. Phys.*, vol. 59, pp. 694–764, 2007.

[11] R. Herman and R. Hofstadter, *High-Energy Electron Scattering Tables*. Stanford University Press, 1960.

[12] L. Andivahis *et al.*, “Measurements of the electric and magnetic form factors of the proton from  $q^2 = 1.75$  to  $8.83 \text{ (gev}/c^2)$ ,” *Phys. Rev. D*, vol. 50, p. 5491, 1994.

[13] A. Puckett *et al.*, “Polarization transfer observables in elastic electron-proton scattering at  $q^2 = 2.5, 5.2, 6.8$ , and  $8.5 \text{ gev}^2$ ,” *Phys. Rev. C*, vol. 96, 2017.

[14] A. Accardi *et al.*, “Electron Ion Collider: The Next QCD Frontier: Understanding the glue that binds us all,” *Eur. Phys. J. A*, vol. 52, no. 9, p. 268, 2016.

[15] P. Achenbach *et al.*, “The present and future of QCD,” *Nucl. Phys. A*, vol. 1047, p. 122874, 2024.

[16] D. W. Higinbotham, A. A. Kabir, V. Lin, D. Meekins, B. Norum, and B. Sawatzky, “Proton radius from electron scattering data,” *Phys. Rev. C*, vol. 93, no. 5, p. 055207, 2016.

[17] M. Goharipour, F. Irani, M. H. Amiri, H. Fatehi, B. Falahi, A. Moradi, and K. Azizi, “Can we determine the exact size of the nucleon?: A comprehensive study of different radii,” *Nucl. Phys. B*, vol. 1017, p. 116962, 2025.

[18] J. Arrington, K. de Jager, and C. F. Perdrisat, “Nucleon Form Factors: A Jefferson Lab Perspective,” *J. Phys. Conf. Ser.*, vol. 299, p. 012002, 2011.

[19] L. N. Hand, D. G. Miller, and R. Wilson, “Electric and Magnetic Form Factors of the Nucleon,” *Rev. Mod. Phys.*, vol. 35, p. 335, 1963.

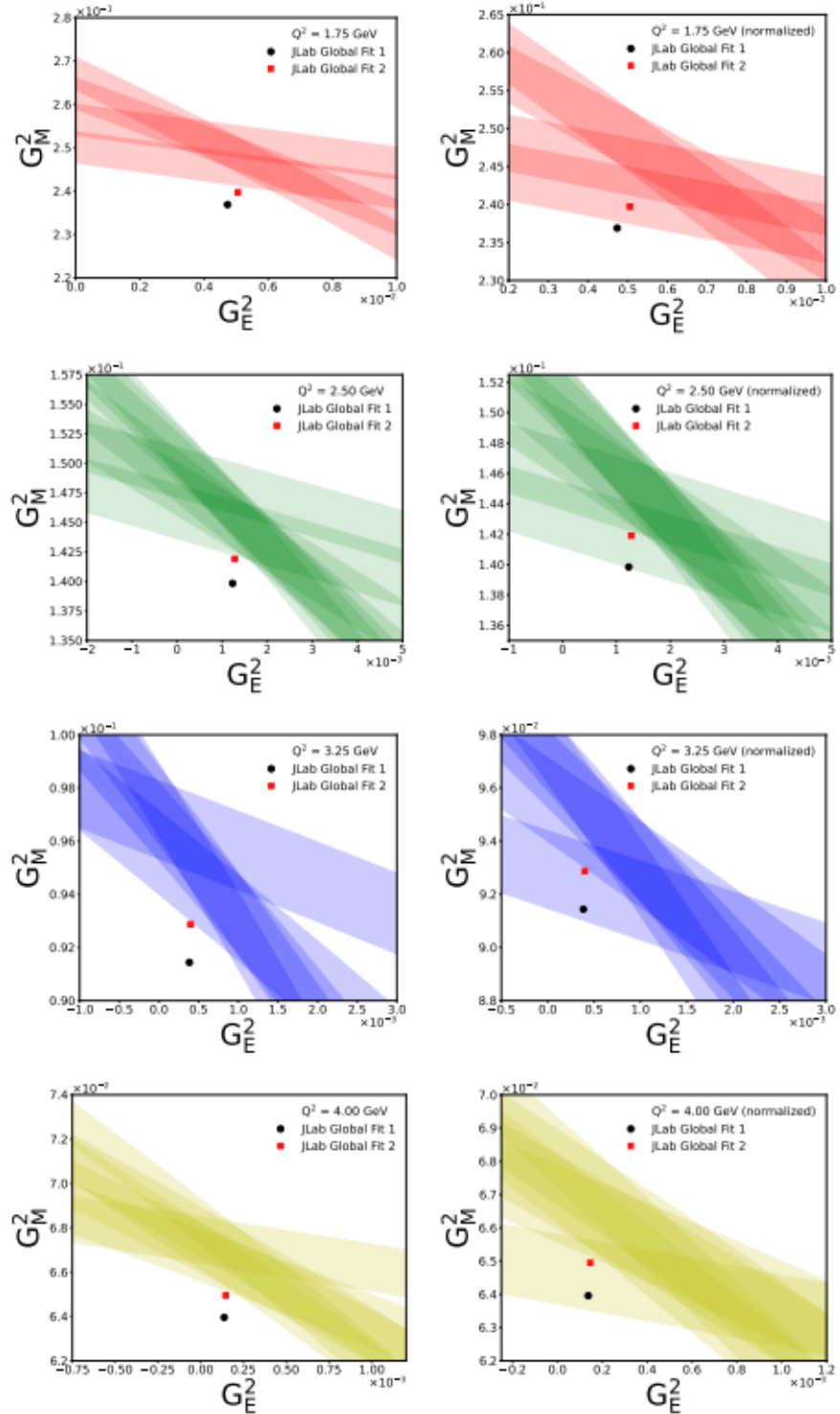


FIG. 7. An 8-panel display of SLAC data for a range of  $Q^2$  values in Hofstadter-Herman format. The left side is the unmodified data, and the right side is adjusted by the 4% normalization applied to the 1.6 GeV spectrometer subset, as in the original 1994 SLAC analysis.

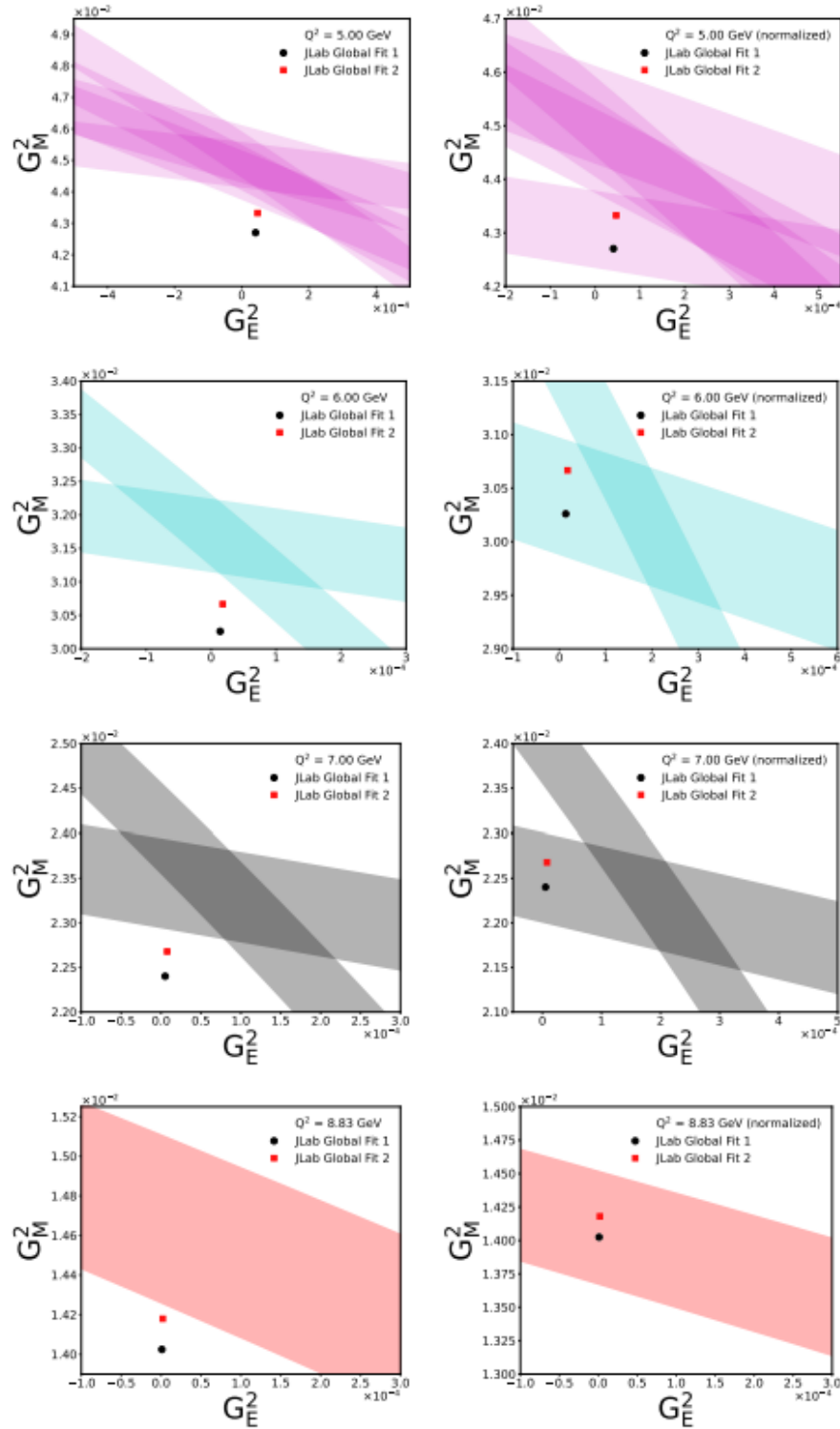


FIG. 8. An 8-panel display of higher  $Q^2$  SLAC data in Hofstadter-Herman format. The left side is the unmodified data, and the right side is adjusted by the 4% normalization applied to the 1.6 GeV spectrometer subset, as in the original 1994 SLAC analysis. The final row in orange shows only one band because SLAC had only one measurement at  $Q^2 = 8.83$  GeV.

$Q^2$	E	$\theta$	$E'$	$\epsilon$	$\frac{d\sigma}{d\Omega}$	$\pm$ Stat. error	$\pm$ Total error
1.75	1.511	90.066	0.578	0.250	$1.440 \times 10^{-1}$	$1.116 \times 10^{-3}$	$1.750 \times 10^{-3}$
1.75	2.407	41.110	1.474	0.704	$1.029 \times 10^0$	$4.715 \times 10^{-3}$	$1.090 \times 10^{-3}$
1.75	5.507	15.145	4.574	0.950	$1.115 \times 10^{+1}$	$6.713 \times 10^{-2}$	$1.336 \times 10^{-1}$
2.50	1.968	89.947	0.636	0.227	$3.389 \times 10^{-2}$	$3.616 \times 10^{-4}$	$4.832 \times 10^{-4}$
2.50	2.407	58.882	1.075	0.470	$9.857 \times 10^{-2}$	$9.199 \times 10^{-4}$	$1.317 \times 10^{-3}$
2.50	2.837	44.993	1.505	0.630	$1.990 \times 10^{-1}$	$1.811 \times 10^{-3}$	$2.368 \times 10^{-3}$
2.50	3.400	34.694	2.068	0.750	$3.951 \times 10^{-1}$	$1.849 \times 10^{-3}$	$4.266 \times 10^{-3}$
2.50	3.956	28.409	2.624	0.820	$6.616 \times 10^{-1}$	$4.025 \times 10^{-3}$	$7.637 \times 10^{-3}$
2.50	5.507	18.981	4.175	0.913	$1.779 \times 10^0$	$1.147 \times 10^{-2}$	$2.120 \times 10^{-2}$
3.25	3.400	61.205	1.105	0.426	$2.848 \times 10^{-2}$	$3.499 \times 10^{-4}$	$4.444 \times 10^{-4}$
3.25	3.956	44.482	1.668	0.609	$6.784 \times 10^{-2}$	$5.949 \times 10^{-4}$	$8.885 \times 10^{-4}$
3.25	4.507	35.382	2.224	0.719	$1.256 \times 10^{-1}$	$1.075 \times 10^{-3}$	$1.636 \times 10^{-3}$
3.25	5.507	22.804	3.775	0.865	$3.898 \times 10^{-1}$	$1.888 \times 10^{-3}$	$4.343 \times 10^{-3}$
4.00	9.800	57.572	1.268	0.437	$1.297 \times 10^{-2}$	$1.858 \times 10^{-4}$	$2.243 \times 10^{-4}$
4.00	3.956	43.707	1.824	0.593	$2.770 \times 10^{-2}$	$3.474 \times 10^{-4}$	$4.407 \times 10^{-4}$
4.00	4.507	35.592	2.375	0.694	$4.929 \times 10^{-2}$	$6.162 \times 10^{-4}$	$7.853 \times 10^{-4}$
4.00	5.507	26.823	3.375	0.805	$1.023 \times 10^{-1}$	$9.097 \times 10^{-4}$	$1.370 \times 10^{-3}$
4.00	9.800	13.248	7.668	0.946	$6.180 \times 10^{-1}$	$4.679 \times 10^{-3}$	$8.073 \times 10^{-3}$
5.00	3.956	59.291	1.291	0.389	$4.205 \times 10^{-3}$	$8.647 \times 10^{-5}$	$9.565 \times 10^{-5}$
5.00	4.507	45.658	1.842	0.538	$8.462 \times 10^{-3}$	$1.239 \times 10^{-4}$	$1.492 \times 10^{-4}$
5.00	5.507	32.829	2.842	0.704	$2.128 \times 10^{-2}$	$2.228 \times 10^{-4}$	$3.079 \times 10^{-4}$
5.00	9.800	15.367	7.135	0.919	$1.576 \times 10^{-1}$	$1.643 \times 10^{-3}$	$2.338 \times 10^{-3}$
6.00	9.800	17.515	6.603	0.886	$4.749 \times 10^{-2}$	$5.879 \times 10^{-4}$	$7.705 \times 10^{-4}$
7.00	9.800	19.753	6.070	0.847	$1.707 \times 10^{-2}$	$3.860 \times 10^{-4}$	$4.249 \times 10^{-4}$

TABLE I. Data provided by the 8 GeV spectrometer at SLAC.

$Q^2$	E	$\theta$	$E'$	$\epsilon$	$\frac{d\sigma}{d\Omega}$	$\pm$ Stat. error	$\pm$ Total error
1.75	1.511	90.066	0.578	0.250	$1.514 \times 10^{-1}$	$3.132 \times 10^{-4}$	$1.690 \times 10^{-3}$
2.50	1.968	89.947	0.636	0.227	$3.545 \times 10^{-2}$	$1.008 \times 10^{-4}$	$4.044 \times 10^{-4}$
3.25	2.407	90.004	0.675	0.206	$1.095 \times 10^{-2}$	$7.314 \times 10^{-5}$	$1.418 \times 10^{-4}$
4.00	2.837	89.966	0.705	0.190	$4.092 \times 10^{-3}$	$3.323 \times 10^{-5}$	$5.636 \times 10^{-5}$
5.00	3.40	89.985	0.735	0.171	$1.339 \times 10^{-3}$	$1.242 \times 10^{-5}$	$1.942 \times 10^{-5}$
6.00	3.956	89.981	0.759	0.156	$5.164 \times 10^{-4}$	$6.577 \times 10^{-6}$	$8.747 \times 10^{-6}$
7.00	4.507	89.991	0.777	0.143	$2.248 \times 10^{-4}$	$5.088 \times 10^{-6}$	$5.675 \times 10^{-6}$
8.83	5.507	90.016	0.784	0.125	$6.022 \times 10^{-5}$	$2.344 \times 10^{-6}$	$2.439 \times 10^{-6}$

TABLE II. Data provided by the 1.6 GeV spectrometer at SLAC.